Journal of Physics and Chemistry of Solids 197 (2025) 112435

Contents lists available at ScienceDirect

Journal of Physics and Chemistry of Solids

journal homepage: www.elsevier.com/locate/jpcs

Strain effect on the physical properties of novel Mg_3NI_3 perovskite material: First principle DFT analysis

I.K. Gusral Ghosh Apurba [a], Md Rasidul Islam [a,*], Md Shizer Rahman [a], Nazia Iram [b], Md Ferdous Rahman [c], Sohail Ahmad [d]

[a] Department of Electrical and Electronic Engineering, Bangamata Sheikh Fojilatunnesa Mujib Science & Technology University, Jamalpur, 2012, Bangladesh
[b] Computational Materials Physics Laboratory, Institute of Physics (IoP), Bahauddin Zakariya University, 60800, Multan, Pakistan
[c] Department of Electrical and Electronic Engineering, Begum Rokeya University, Rangpur, 5400, Bangladesh
[d] Department of Physics, College of Science, King Khalid University, P O Box 9004, Abha, Saudi Arabia

ARTICLE INFO

Keywords:
Perovskite
Optical properties
Poisson's ratio
Tolerance factor
Spin-orbital coupling effect
Bulk modulus
And anisotropic factor

ABSTRACT

Inorganic perovskite-based substances have become a major attraction to solar technology. Inorganic cubic Mg_3NI_3 perovskites have generated a heap of fascination owing to their distinctive optical, electrical, and structural features. The photovoltaic and optoelectronic industries prioritize lead-free, atomically tailored metal halide perovskites due to the need to address lead (Pb) toxicity and instability. This study assessed the optical, structural, and electrical parameters of Pb-free inorganic halide perovskites Mg_3NI_3 as a function of biaxial compressive and tensile strain, leveraging first-principles density-functional theory (FP-DFT). Refractive index, absorption coefficient, reflectivity, dielectric function, and tolerance factor are a few additional optical parameters that are computed and processed. The bandgap of the planar Mg_3NI_3 molecule is 0.412 eV (PBE) when SOC is not applied. The bandgap reduces to 0.363 eV (PBE) at its Γ(gamma) and R-point when the subjective SOC effect is taken into consideration. This compound's bandgap will narrow under tensile strain and expand under compressive strain, depending on whether the SOC effect is applied or not. Several elastic factors are anticipated, including the bulk modulus, Pugh's ratio, elastic constants, anisotropic factors, and Poisson's ratio. Electronic property calculations using band mechanism and density of states (DOS) suggest that Mg_3NI_3 have a bandgap that is indirect and semiconductive. The elastic properties of this material were found to be mechanically stable, anisotropic, and ductile. In the photon energy range suitable for solar cells, the spikes in the dielectric constant of Mg_3NI_3 are seen. Our findings point to the prospect of Mg_3NI_3 as a non-toxic, high-performance, low-cost material for implementation in solar cells and different semiconductor devices.

1. Introduction

The field of photovoltaics has seen astounding developments with perovskite materials, which are considered possible substitutes for high-efficiency solar cell technologies [1–5]. Many individuals are still captivated by inorganic perovskites due to their distinctive and captivating optical, electrical, and structural features. Different perovskites from the A_3MX_3 group have emerged as promising new additions to this class of materials. Hybrid organic-inorganic perovskite solar cells (PSCs) have superior photovoltaic (PV) efficiency compared to conventional cells [6–11], due to their reduced trap density, increased optical absorption, decreased exciton binding energy, improved charge-carrier mobility, and longer charge-carrier lifespan [12–14]. Solar cell materials such as CdTe, CIGS, Sb_2Se_3, CMTS, and $FeSi_2$ have achieved great progress in the PV area [15–23], however, due to the customized traits that they possess, perovskites have recently garnered the interest of researchers [5,12,14]. In spite of their thin layer thickness, perovskites are more efficient in photon capture than other semiconductors [21,24–26]. The power conversion efficiency (PCE) of perovskite solar cells has escalated from 2.9 % in its early stages to over 19 % in recent years, drawing a lot of interest in these cells [27,28]. A collaboration with organic-inorganic perovskites (OILHP) allowed solar cells to achieve a PCE of 26.1 % in 2023 [29].

Although they have these advantages, their instability keeps them from being widely applied [25]. In real-world situations, the stability of these perovskites is highly unstable due to their extreme sensitivity to

---

* Corresponding author.
E-mail address: rasidul@bsfmstu.ac.bd (M.R. Islam).

https://doi.org/10.1016/j.jpcs.2024.112435
Received 17 August 2024; Received in revised form 15 October 2024; Accepted 2 November 2024

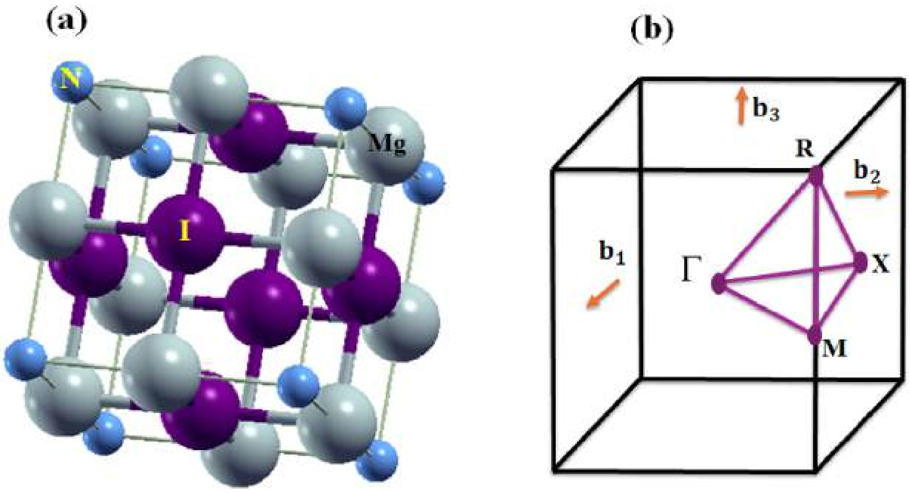

Fig. 1. (a) The optimal structure of Mg_3NI_3 and (b) the k-path of the first Brillouin zone to determine its electronic band configuration.

variations in temperature, humidity, light, and air [26]. Therefore, research into commercially viable, high-efficiency inorganic halide perovskite (IHP) materials must be given top priority by the solar cell industry. Strain engineering is a powerful tool for tailoring perovskite materials to solar applications by altering their physical properties and crystal structure. New studies show that perovskite material's structural properties are influenced by the amount of strain applied to them [30–36]. There have been attempts to create a lead-free perovskite, but the levels are still much lower than the levels of lead-based perovskites [37–41]. Commercializing photovoltaic materials with zero lead content and outstanding productivity has thus become the principal goal of the solar cell industry [42]. As a material belonging to the A_3MX_3 family, it contains the following elements: $M = P^{3-}/As^{3-}/N^{3-}/Sb^{3-}$, $X = F^-/Cl^-/Br^-/I^-$, and $A = Mg^{2+}/Ca^{2+}/Sr^{2+}/Ba^{2+}$. It resembles cubic halide perovskites in structure and conveys superior parallelism with the Pm-3m (no. 221) space group [6–8,10,11,43]. Because of its photovoltaic uses, this material's parity allows for band-edge state changes [44]. Solar cells are one possible future optoelectronic and electrical products that could make use of this material. According to A. K. Hossain et al. the inorganic perovskite $CsSnCl_3$ exhibits remarkable optoelectronic properties and transforms dramatically from a semiconductor to a metal architecture [39]. Furthermore, it was discovered by D. Liu et al. [40] that compressive or tensile strain can dramatically change the $CsGeI_3$ perovskite's bandgap characteristics and dielectric function.

Numerous advantageous characteristics of Ca_3PI3 and Ca_3AsI_3 were noted in earlier research [11,41,42], making them materials with promising potential for use in solar cell technology. These materials can compete with other materials used in photovoltaic applications. In a similar vein, we find that Mg_3NI_3 exhibits the expected bandgap at an energy concentration suitable for solar reception and that the compound is effectively converting photons to electrons. Because of this quality, Mg_3NI_3 can absorb more light across a wider range of wavelengths than other materials, enabling it to harness more of the sun's energy than other options. The crystal structure of Mg_3NI_3 is stable, and it has a substantial tolerance aspect and dynamic equilibrium, both of which contribute to its excellent transport ability and stronger carrier transit and collection. Therefore, solar cells and other electronic and optoelectronic devices will soon be able to utilize this material. As far as we know, no investigation has reported the electrical as well as optical characteristics of Mg_3NI_3 following contemporaneous exposure to strain and spin-orbit coupling (SOC). This investigation extensively finds the electrical and optical traits of Mg_3NI_3 to evaluate the influence of external strain.

The DFT technique is employed to achieve this objective. The study focused on the customization of the bandgap, band structure, electron charge density, and stability in Mg_3NI_3. A thorough investigation of the electronic properties of Mg_3NI_3 is performed as it pertains to the implications of the outer strain on the structural features and energy gap. The investigation also finds the characteristics of Mg_3NI_3's absorption spectra, with a particular focus on the shift of the dielectric's most severe points in the red and blue domains because of variable strain conditions. Thus, this investigation verified the stability of Mg_3NI_3 perovskite, bandgap, optical properties, and investigate its mechanical properties. In a nutshell, the results indicate that Mg_3NI_3 could be customized for use in solar energy and optoelectronics by modifying its photonic properties.

2. Computational details

A norm-conserving (NC) pseudopotential and the Perdew-Burke-Ernzerhof (PBE) exchange-correlation function was implemented to assess the Mg_3NI_3 material employing the FP-DFT [43,44]. The Quantum Espresso (QE) simulation tool is used to perform the first-principles computations [43,44]. By setting the kinetic energy and charge density cut-off at 50 Rydberg (Ry) and 440 Rydberg (Ry), enhancements in structure and execution have been exceeded. The self-consistency functional was calculated using a convergence threshold of about 10^{-6} a. u. And the greatest strength tolerance of below 0.01 eV/ A°. Additionally, relaxation calculations for ionic minimization used a force convergence threshold of about 10^{-4} a. u. According to Ref. [45], the band structure and PDOS were computed in the Brillion zone using the Monkhorst-Pack k-grid at $6 \times 6 \times 6$. In AIMD calculation we use 60,000 is the total number of steps at 300 K temperature. Using functionals such as local density approximation (LDA) and generalized gradient approximation (GGA), certain organic halides were calculated, and it was demonstrated that the absolute mean error exceeds 10 p.m. [46]. In our most current investigations, we have refrained from using corrected PBE functions for metals, even though there are methods to mitigate this problem [47,48]. The Heyd-Scusena Ernzerhof (HSE-06) hybrid function was employed as well to provide more precise bandgap estimations for these perovskites. The optical characteristics of the perovskite structure were studied by evaluating their complicated dielectric functions that rely on photon energy (eV) once dynamical stability had been achieved. The spectral features were computed using Quantum Espresso and the first-order time-dependent perturbation theory [49].

The biaxial compressive and tensile strains can be determined by adjusting the lattice parameter $a_{strained}$, as shown in equation (1) below [10]:

$$\varepsilon = \frac{a_{strained} - a_{relaxed}}{a_{relaxed}} \times 100\% \tag{1}$$

Table 1
Mg_3NI_3 material lattice constant and energy bandgap were determined using investigational data using DFT calculations.

Structure	Lattice Constant (A)	This work Bandgap Energy (eV)		Previous work Bandgap Energy (eV)	Tolerance Factor	Effective Mass ($m_0 = 9.1093$ $\mathbf{10^{-31}}$) Kg	
						Electrons	Holes
Mg_3NI_3	5.60	0.412 (PBE)	0.869 (HSE)	1.03 (HSE) [88]	0.995	$0.9514m_0$	$0.4124m_0$

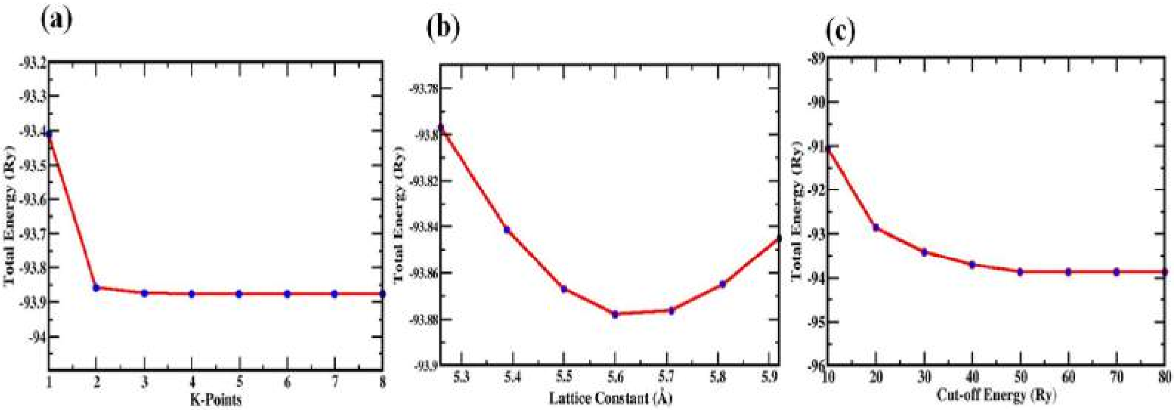

Fig. 2. Variation of Mg_3NI_3 per unit cell total energy concerning (a) k-points, (b) lattice constant, and (c) cut-off energy.

We remark that the lattice constant is $a_{relaxed}$ when no pressure exists. The value of ε is between −6% and +6 %, with each unit representing 2 %. While compressive strain is indicated when ε is negative, tensile strain is indicated when ε is positive. Using first-order time-dependent perturbation modelling, the aesthetic qualities and dynamic sustainability of the material configurations were examined [46,47]. We have retained a gamma-centered 8 × 8 × 8 Monkhorst-Pack k-mesh patterns for evaluating the optical traits. The complex dielectric equation was then studied to determine the range of photon energy (eV) in which its absorption maxima were detected.

3. Results and discussion

3.1. *Structural properties*

The periodic pattern of Mg_3NI_3 is the Pm3 m cubic basis. The single cell of the arrangement shown in Fig. 1(a) divides into seven components. This material contains a configuration of Mg and N atoms in a cubic lattice, with the face-centered and I atoms occupying an octahedral space. The bond distances of Mg_3NI_3 for Mg–N and Mg–I are surveyed at 2.8059 A° and 2.8059 A°**.** To form NMg_6 octahedra that share corners, six similar Mg^{2+} atoms are connected to N^{3-}. The octahedra, without a corner, share a common space. Mg, N, and I are fractional coordinates of (0.5,0.5,0), (0.5,0.5,0.5), and (0.5,0,0), respectively; to find these coordinates, use the 1a, 3c, and 3d Wyckoff sites. The k-path linked to the first Brillouin zone appears in Fig. 1(b). Understanding the structural features of Mg_3NI_3 perovskite is significant before determining its different properties. By employing PBE, the structural features, involving the lattice constant (A°), were evaluated; the findings appear in Table 1. The lattice constant with the highest reliability of Mg_3NI_3 is found by evaluating the total energy while considering the lattice parameter.

An independent variable, the lattice parameter, is utilized for obtaining a projection of the total energy with the aim of picking out the optimum lattice constant for the Mg_3NI_3 material. The total energy may have been driven by a change in the lattice constant, as depicted in Fig. 2 (b). The relaxed Mg_3NI_3 structure has the smallest total energy of 5.60 A°, which is in reasonably good agreement with the findings of the previous quantitative and practical studies listed in Table 1 [50]. The parameters that determine the optimal structure are the lattice constant,

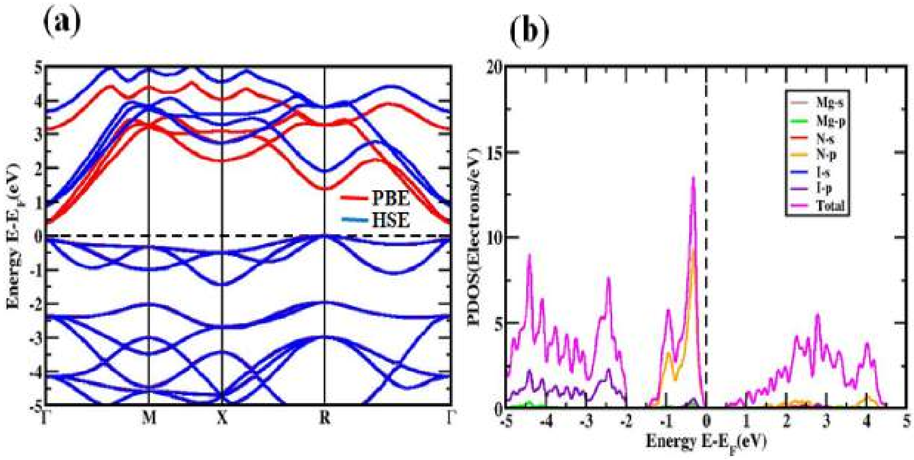

Fig. 3. Mg_3NI_3 perovskite structure without SOC (a) the electronic band formation and (b) PDOS.

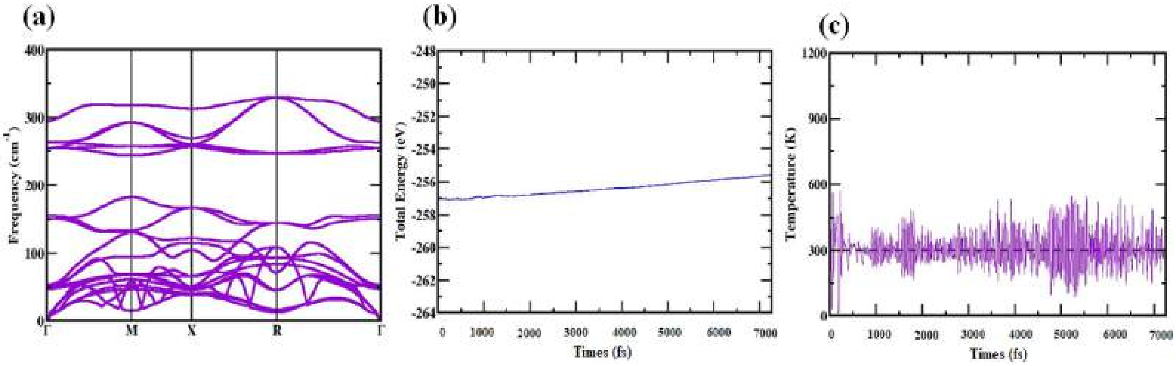

Fig. 4. (a) The Phonon band structure of Mg_3NI_3 Compound. Variation of Total energy (b) and Temperature (c) with respect to time for Mg_3NI_3 material during AIMD simulation.

the kinetic cut-off energy, and the variety of k-point items in the circular loop in the Brillouin zone (BZ). We also investigated the total energy by adjusting the plane wave's k-values and cut-off energies in the context of the PBE pseudopotential of the standardized valley assumption. Fig. 2(c) shows that the total energy converges, implying that a kinetic cut-off of 50–80 Ry is effective for delineating the Mg_3NI_3 material. Establishing relative stability necessitates enough k-point sampling, and as can be presented in Fig. 2(a)–a k-point mesh of 6 × 6 × 6 is acceptable for this compound.

A computed lattice value of 5.60 A° indicated that the optimum compound of Mg_3NI_3 is one popular metric for gauging progress in perovskite structure development, which is the Goldschmidt tolerance factor. The solution manifests as equation (2):

$$t_G = \frac{r_{Mg} + r_I}{\sqrt{2}(r_N + r_I)} \tag{2}$$

Scientists [50] observe that material will have structural stability if the tolerance factor exists throughout the spectrum. *of* $0.8 < t_G < 1.0$. The Shannon ionic radii of these ions are represented by r_{Mg}, r_N and r_I. We may anticipate that this compound will crystallize in the cubic perovskite phase since their tolerance factors for Mg_3PI_3 is 0.995, in where r_{Mg} is 150 p.m., r_N is 65 p.m., and r_I is 140 p.m. [51]. within the range that allows the development of the perovskite structure, which is defined as $0.8< t_G <1.0$. Thus, it is a highly stable substance.

3.2. *Electronic properties*

Band structure, density of states (DOS), and the density of charges are the primary predictors of the electrical properties of a material [64]. For Mg_3NI_3 perovskite structures, the electronic band attributes, and high equipoise directions have been approximated. An electronic band arrangement of the Mg_3NI_3 framework is apparent in Fig. 3(a). The bandgap value can be conveniently evaluated with the Fermi levels set to zero. The cubic structure's Γ-*M*-X-R-Γ is aligned with the k-axis. The conduction band minimum (CBM) and valence band maximum (VBM), located around the Γ (Gamma) and R-points, appear in Fig. 3(a). Predictions for the Mg_3NI_3 perovskite's bandgap structures using the PBE/HSE function predict values of around 0.412 eV/0.869 eV. This result is generally consistent with previously reported results [50,51]. When the bandgap is measured using the GGA approach, it is common for the bandgap value to be clearly understated. Additional evidence of bandgap undervaluation is found in the (LDA) + U and LDA local density approximation addresses [52]. The GW tackle hybrid functional represents one of the many techniques proposed by experts [53] for avoiding bandgap estimations of this kind.

All things considered, the PDOS reveals that distinct molecular topologies alter the bandgap energy of the Mg_3NI_3 composition. Fig. 3(b) shows the spatial distribution of PDOS in Mg_3NI_3 from −5 to 5 eV. It has been found that the bandgap is conserved across the whole spectrum of energy in the Mg_3NI_3 hybridized Mg and N forms. This confirms that covalent bonds are the most basic type of bond between Mg–I and *N*–I. The movement of electrons across Mg and N to I in Mg_3NI_3 is also implicated, as shown in Fig. 3(b), which may have been caused by the substantial disparity in atomic states. Beyond the Fermi level, the Mg atom involvement is simply nonexistent. The density of states around the I-2p orbital-dominated valence band of Mg_3NI_3 is the main topic of our cubic phase article. Also important in the conduction band are the N-2p and, to a lesser degree, the Mg-3s orbitals.

For the determination of the effective mass of electrons and holes from the band diagram we use the formula, $m^{*}(\mathrm{k}) = \overline{h}^{2}3\left(\partial^{2}\,\mathrm{E(k)}/\partial\left(k^{2}\right)\right))^{-1}$, where m*(k), E(k), k, and $\overline{h}$, are the effective mass, energy, wave vector, and reduced Planck's constant, respectively Our calculated effective mass for the holes in Mg_3NI_3 is $0.412m_0$ at R-point. For the complex Mg_3NI_3 the effective mass of the electrons is $0.951m_0$ at Γ point, respectively, where $m_0 = 9.1093 \times 10^{-31}$ Kg. Previous research found that the range of $(0< m_h^* <m_e^* <1)$ where the electron's effective mass is m_e and holes effective mass m_h [54].

3.3. *Structural stability*

The association between momentum and phonon energy is described by using the term "phonon dispersion" when addressing phonons in a crystal lattice. As they traverse a material, phonons, which are quantized vibrations of its lattice, influence its mechanical and thermal attributes. During the phonon estimation, the lattice volume and atomic positions are entirely relaxed [55,56]. The initial Brillouin zone, along the high-symmetry domains Γ-*M*-X-R-Γ, shapes the phonon band of the Mg_3NI_3 molecule. Fig. 4(a), the dispersion mapping, must be analyzed to figure out the ongoing stability of the substance. This map validates that the evolving matrix excludes any negative frequencies for proximity.

Ab initio molecular dynamics (AIMD) simulations have been extensively studied in solid electrolyte materials [55–57]. The substantially occupied component of the well-known solid electrolyte material Li_6PS_5Cl (argyrodite) [57–65] presents arrangement difficulties when creating the input model framework for use in DFT and AIMD computations. Through AIMD models, we can explore how electronic band gaps fluctuate based on structural traits and the relevance of long-range dispersion interactions. For the sole purpose of assessing AIMD functions at ambient temperature (300 K), Fig. 4(b, c) shows the outcomes of the AIMD simulations, revealing further evidence that Mg_3NI_3 is thermally stable. It appears that the energy and temperature metrics disclose extremely slight changes as time increases, and there is no large structural shift nearer the end. Fig. 4(b) depicts the total energy opposed to time interactions, while Fig. 4(c) shows the temperature versus time intimacy.

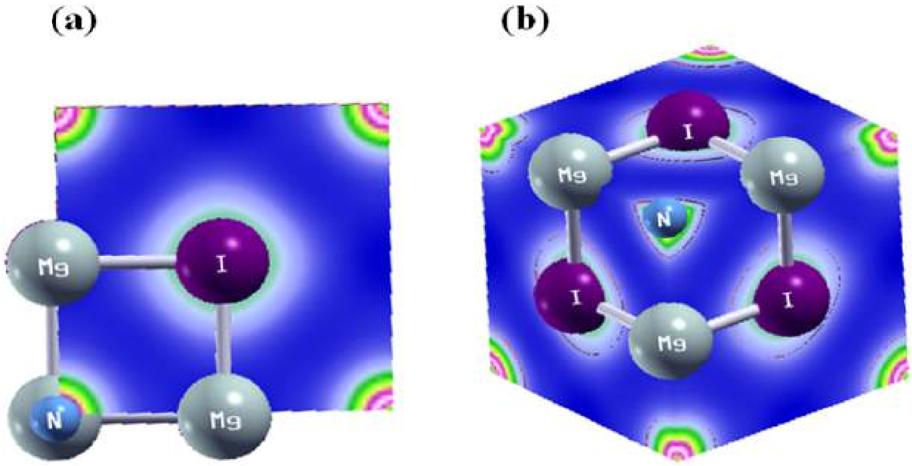

Fig. 5. An analysis of the electronic charge distribution in Mg_3NI_3 (a) A two-dimensional depiction of the (200) plane and (b) A three-dimensional viewpoint.

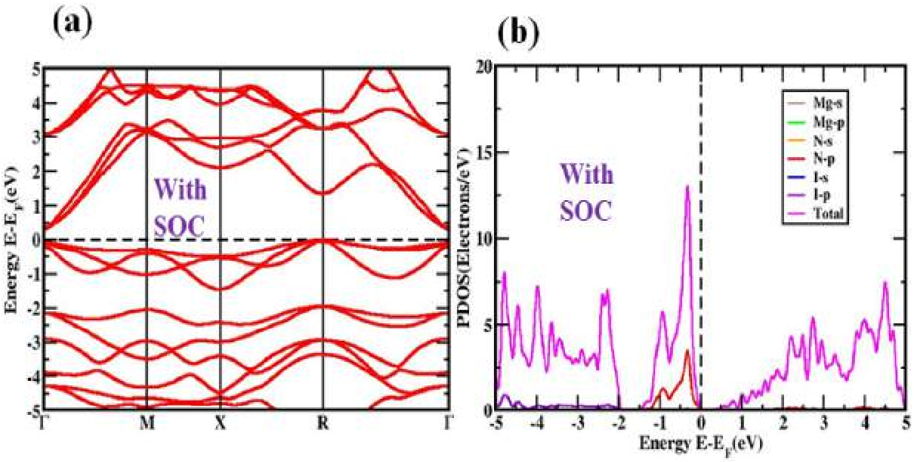

Fig. 6. Mg_3NI_3 perovskite structure with SOC (a) the electronic band formation and (b) PDOS.

3.4. Charge density

The charge density of Mg_3NI_3 in two dimensions correlated to the (200) crystalline plane, portrayed in Fig. 5(a). When seen in this light, the intense distribution of charges around the atoms is clearly visible. Fig. 5(b) provides a three-dimensional representation. The primary site of charge clustering is typically the magnesium atom. Furthermore, the charges are consistently ordered. The I atom had a smaller array of charges surrounding it. Because the charges of the Mg and N ions overlapped, it was not possible to examine the N atom in the individual charge distribution that was envisioned, leading to the formation of a covalent bond between the two ions [48,67,68]. Additionally, the fact that the charge contours of Mg and I do not coincide [66–68] suggests that, concerning the charge distribution, the ions establish an ionic connection. To reinforce its bonding nature, the structure relies on the ionic bond; to create a weaker link, the covalent linkage of Mg and N ions is used. N and I both have anti-bonding inclinations.

3.5. The effect of SOC on electronic structure

We used the SOC-containing Hamiltonian equation to study its effects on the Mg_3NI_3 perovskite's electrical characteristics. Equation (3) is utilized to H_{soc}

$$H_{soc} = \frac{\hbar}{4m_0c^2}\left(\overrightarrow{F} \times \overrightarrow{p}\right) \cdot \overrightarrow{s}. \tag{3}$$

Table 2
The calculated bandgap of cubic Mg_3NI_3 perovskite under different compressive and tensile strains.

Applied Strain (%)	Mg_3NI_3			
	Compressive		Tensile	
	Without SOC	With SOC	Without SOC	With SOC
0	0.412	0.363	0.412	0.363
2	0.604	0.530	0.299	0.226
4	0.774	0.709	0.180	0.122
6	0.985	0.946	0.079	0.048

The Hamiltonian operator that considers SOC is marked by H_{soc}, where $\hbar$ is the reduced Plank's constant, p→ stands for orbital angular momentum, F→ is the force or potential energy, m_0 is the mass of unbound electrons, and s→ is the spin angular momentum. Using relativistic investigations centered on the PBE functional approach, we were required to identify the translational influence scale to explain how heavy elements Mg and N alter the electrical properties of Mg_3NI_3 perovskites having SOC. According to Fig. 6, the CBM and VBM positions were drastically altered because of SOC's effect on the areas of the conduction and valence bands. The VBM underwent notable modifications as it rose, whereas the CBM dropped towards the Fermi level. At 0.363 eV, Mg_3NI_3 has a bandgap energy value due to the SOC effect. As shown in Fig. 6(a), the SOC consequence also leads to a fall in bandgap

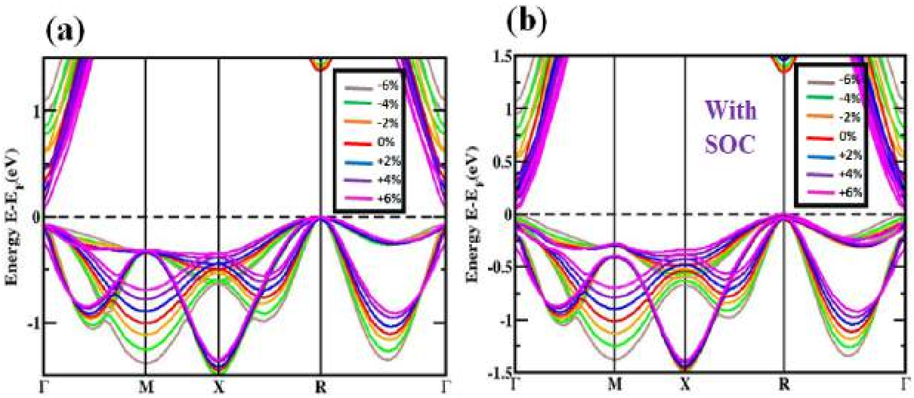

Fig. 7. Mg_3NI_3 electronic band structure with biaxial strain (a) without SOC and (b) with SOC effect.

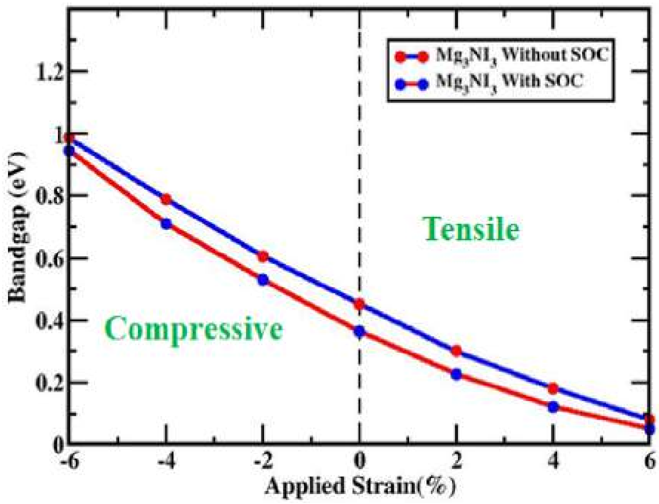

Fig. 8. The variation of Mg_3NI_3 electronic band structure bandgap with biaxial strain for both with and without SOC effect.

value in the Mg_3NI_3 perovskite formations. Bearing into consideration or ignoring the SOC effect, the bandgap energies of the Mg_3NI_3 materials are shown in Table 2.

The cubic Mg_3NI_3 band arrangement and its changes in bandgap were more evident when we took into account the impact of SOC while examining the relevant PDOS. When SOC is present, the PDOS, as seen in Fig. 6(b), has no discernible pattern in how it affects the magnesium atoms. At regions with great symmetry, the band edge separation caused by the SOC effect does not manifest as I-5p into p (j = 1/2) and I-5p into p (j = 3/2) splitting apart. In the VB, the energy spectrum of −5 to 0 eV is mostly influenced by the I-5p (j = 1/2) and I-5p (j = 3/2) atoms, as seen in Fig. 6(b). Contrarily, N-3p (j = 1/2) and N-3p (j = 3/2) are mostly responsible for the energy on the CB portion, which spans from 0.5 to 4.5 eV.

3.6. Strain-dependent electronic properties

Using strain as a percentage, we evaluated the implications of surface area ratio (SOC) on compressive and tensile stresses on the arrangement of Mg_3NI_3, both with and without SOC. The range of planned compressive to tensile strain covers a pressure that is between −6% and +6 %, with 2 % increments throughout. Fig. 7(a) shows that the VBM and CBM for perovskites with concentrations of Mg_3NI_3 reach the Fermi zone when compressive and tension strain are employed. Fig. 7(b) shows the band structures of Mg_3NI_3 that handle the SOC impact while simultaneously experiencing tension and compression strain, correspondingly. The compressive strain increases the bond width between the Mg_3NI_3 atoms, causing orbits to become more crowded (not considering the SOC effect).

The positions of the VBM and CBM between the R and Γ-point for Mg_3NI_3 appear to be of considerable significance under the imposed compressive strain, spanning from −6% to 0 %. The linear bandgap for Mg_3NI_3 is obtained at the R to Γ-point, irrespective of whether the SOC effect is utilized or not. The bandgap is shown to have been formed by an increase in compressive strain, demonstrating this both inside and outside of the SOC impact. A tensile strain applied in a range of 0 % to +6 % additionally affects the electrical band's composition. The VBM

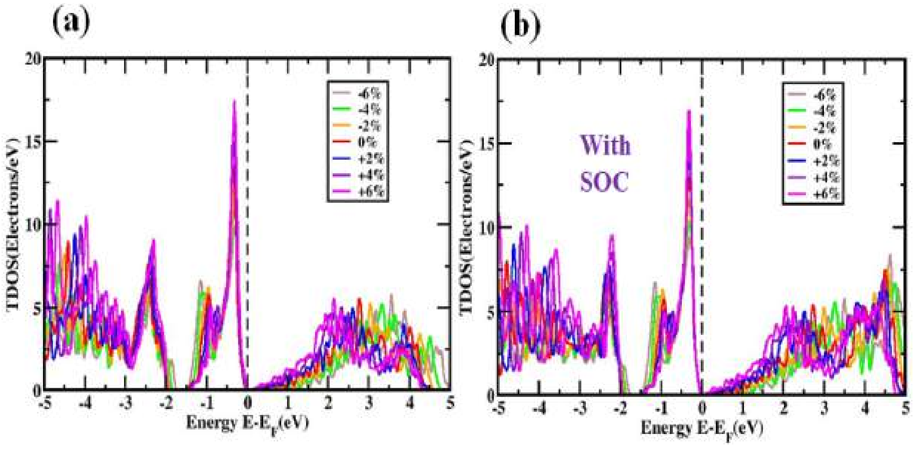

Fig. 9. The TDOS values of Mg_3NI_3 are almost at Fermi levels in various strains without (a) and with SOC consequence (b).

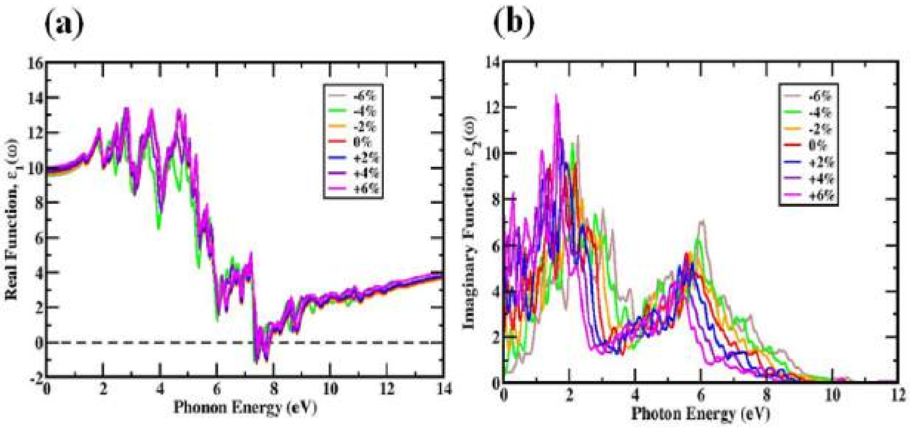

Fig. 10. (a) The real and (b) imaginary dielectric constant with respect to different biaxial strains.

and CBM for these cases have diverged from the Fermi level due to the incorporation of tensile strain. The band gap in the structures of Mg_3NI_3 narrows under tensile strain. Upon careful investigation of the SOC effect in the Mg_3NI_3, it is worth noting that a linear bandgap has been discovered between the R and Γ-point. An indirect bandgap in the electronic band arrangement is seen in the Mg_3NI_3 compound because of compressive and tensile strain. The bandgap deviations for the Mg_3NI_3 materials during compressive and tensile consumption, with and without the SOC effect, appear in Table 2 and Fig. 8, correspondingly. The bandgaps of Mg_3NI_3 varied from 0.985 to 0.079 eV (not using SOC) and 0.946 to 0.048 eV (with SOC) in the used strain range of −6% to +6 %. Across the whole applied strain limit, the indirect bandgap properties for Mg_3NI_3 remain surprisingly unmodified. This means that these structures could be able to use the ideas provided in Shockley-Queisser's theory [69] to boost solar cell productivity.

Fig. 9 displays the TDOS for Mg_3NI_3 in multiple combinations without and with the interplay between SOC and biaxial strain. Understanding the configuration of the electronic band's dynamics in Mg_3NI_3 can be substantially improved with the assistance of TDOS analysis. The existence of SOC has no bearing on the valence band, which agrees with the Fermi level in the unstrained Mg_3NI_3 in TDOS, which is mostly governed by the orbitals of the I atom. The Mg-3p and N-3p orbitals carry minimal influence. Additionally, the N atomic orbitals still have little effect on the TDOS of the conduction band even when SOC is present, but the Fermi level and the Mg-3p and -5p orbitals produce an enormous difference. According to the outcomes of Nayak et al. the absence of a DOS proximity line to the Fermi level reveals the material's bandgap and semiconductor characteristics. No link between this effect and the functional exchange coefficient used [70] has been discovered.

Because compressive stresses within 0 % and −6% drive the emergence of the TDOS line near the Fermi level. The conductivity of Mg_3NI_3 materials diminish as an outcome of the TDOS line, which exceeds the Fermi level at tensile strain spanning 0 % to +6 %, even when the SOC effect is intact. After taking an in-depth look at the band arrangement and DOS of the Mg_3NI_3 materials, it is to be anticipated that the bandgap will fluctuate.

3.7. Optical properties

This item delves into the optical characteristics of Mg_3NI_3, including optical loss, optical absorption, and both the imaginary and real elements of the dielectric function. An assortment of strains, ranging from −6% to +6 %, were employed to conduct this study.

$$\varepsilon(\omega) = \varepsilon_1(\omega) + i\varepsilon_2(\omega) \tag{4}$$

Based on equation (4), the dielectric parameter ε(ω) is composed of two parts: the real part, $\varepsilon_1(\omega)$ and the imaginary part, $\varepsilon_2(\omega)$ [71]. Parts of the momentum matrix are implemented for identifying the imaginary section of the dielectric property, while the Kramers-Kronig revision is used to gain the real part [74,75].

The real components of the unstrained and strained Mg_3NI_3 dielectric constants for photon energies up to 14 eV are shown in Fig. 10(a). Making use of the dielectric function's actual aspect has shed light on the connection between polarization and scatter consequences. To understand the ocular features of a material, one must consider the electronic component of its dielectric function, indicated as $\varepsilon_1(0)$, that occurs at zero frequency. A value of 9.71 is assigned to $\varepsilon_1(0)$ for cubic Mg_3NI_3. As it increases from $\varepsilon_1(0)$ to its highest possible value, the real part of the dielectric function $\varepsilon_1(\omega)$ shows a progression. Remarkably, in the true part $\varepsilon_1(0)$ of the dielectric function, discrete peaks of absorption appear around photon energies is about 3.68 eV for Mg_3PI_3. Thereafter, it settles out and produces several peaks. Modifying the biaxial strain has altered the dielectric constant peaks of Mg_3NI_3. As the tensile strain boosted the Mg_3NI_3 the structure showed a redshift regarding lower photon energy owing to a lower bandgap and a higher peak dielectric constant [72]. On the other side, Mg_3NI_3 observed a blueshift towards larger photon energy resulting from a decreasing peak dielectric constant as compressive strain increased.

The movement of the unreal dielectric constants $\varepsilon_2(\omega)$ during both unstrained and strained situations may be noticed in Fig. 10(b). The imaginary dielectric constant $\varepsilon_2(\omega)$ has offered us information regarding the electronic bandgap. An extensive range of absorption spectra can be identified by the values of $\varepsilon_2(\omega)$ for Mg_3NI_3. Fig. 10(b) shows that at the optical maxima level of 9.55, the main peak for $\varepsilon_2(\omega)$ is observed at a photon energy of 2.18 eV when there is no strain applied. The peak of the dielectric function's imaginary portion moves into the low-energy area owing to strain, which causes it to sharply climb. At photon energies greater than 12 eV, in the case of all strain-modulated Mg_3NI_3 samples, the imaginary portion of the dielectric characteristic is zero. In this region, the strain-modulated samples have superb optical transparency and very low optical absorption, as there is no $\varepsilon_2(\omega)$ greater than 12 eV. A transition from the valence to the conduction spectrum is characterized by peaks in the imaginary region of the dielectric constant, resulting in changes to the peak locations. A redshift transpired at higher photon energies (blueshift) when resulting compressive, and a tensile strain shift occurred at lower photon energies (redshift) when tensile strains increased, respectively. Biaxial tensile and compression over a wide spectrum of energies greatly impact the absorption spectra of Mg_3NI_3, as indicated by this research [72].

A material's light-absorbing potential is assessed by its optical absorption coefficient. A solar cell's PCE can be upgraded with the help of the information it delivers. For this scenario, the coefficient of optical absorption maintains the identical rhythm as the imaginary part of the

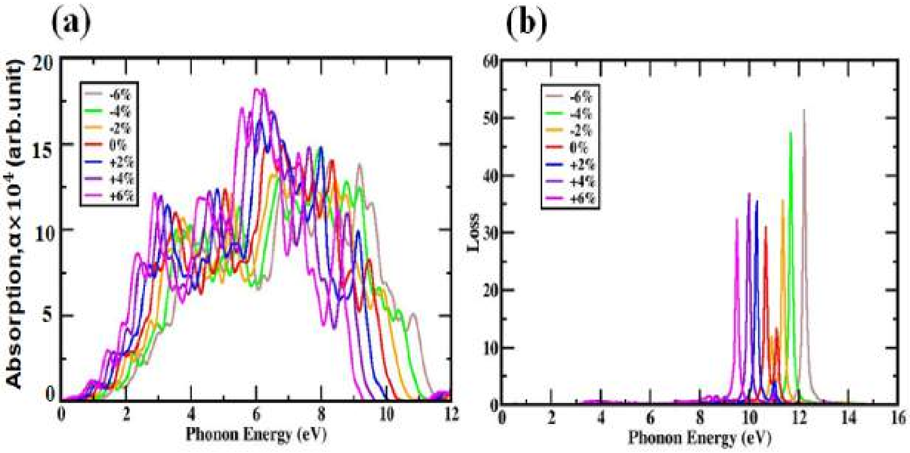

Fig. 11. (a) Absorption coefficient and (b)loss function as a function of photon energy with respect to both compressive and tensile strains.

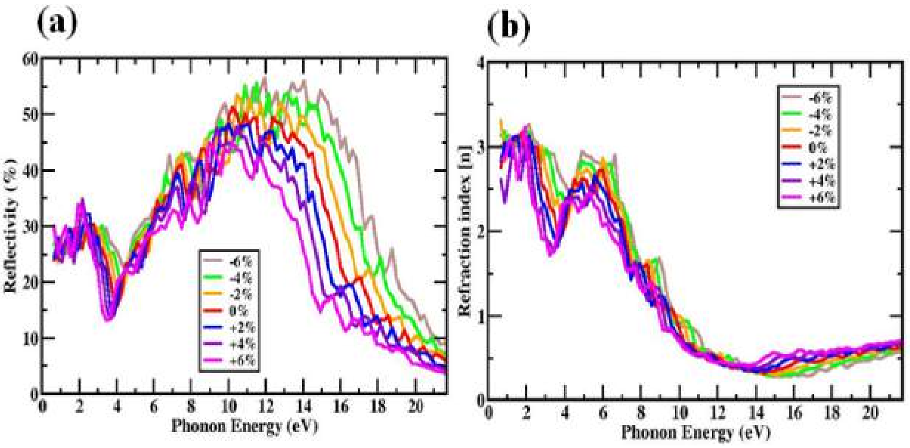

Fig. 12. Reflectivity (a) and reflective index [n] of Mg_3NI_3 for both compressive and tensile strain.

dielectric function. The optical absorption patterns of Mg_3NI_3 reveal their greatest peak in the visible region. Under both unstrained and distinct biaxial strains, Fig. 11(a) shows the Mg_3NI_3 absorption coefficient as a function of the energy of photons. Its absorption pattern shows that the edge reveals a significant redshift under compressive strain and a major blueshift under tensile tension. Compared to their unstrained counterparts, structures subjected to compressive strain have superior visible light absorption properties. The schemes differ from the previous instance under tensile strains. The anticipated bandgap is commensurate with Mg_3NI_3's strain-modulated absorption change. An elevation of compressive strain is a crucial property for utilization in solar cells, which causes the apparent absorption coefficient of the Mg_3NI_3 structure to go up. Raising tensile strain drives Mg_3NI_3 apparent absorption coefficient to drop. When electrons travel via a dielectric, their energy can be determined by the electron loss function. A representation of it is given by equation (5) [73],

$$L(\omega)=\frac{\varepsilon_2(\omega)}{\varepsilon_1^2(\omega)+\varepsilon_2^2(\omega)} \tag{5}$$

One essential tool to investigate a material's light-dependent response is the energy loss mechanism, or L(ω). It calculates the energy passage loss within the barrier or substance. Energy loss takes place when the incoming photon energy approaches the material's bandgap, as seen by the peaks in the L(ω) graphs for Mg_3NI_3. The L(ω) peaks for the cubic configuration of Mg_3NI_3 are seen between 8.83 eV and 11.63 eV, when strain is not present, which is displayed in Fig. 11(b). It is difficult to see dispersions at energies lower than the bandgap. For photon energies up to 13.46 eV, the loss function of strain-induced Mg_3NI_3 is identified. In Fig. 11(b), we can see the optical loss of Mg_3NI_3 under different tensile and compressive strain situations. In all structures, tensile strain results in a redshift, or a shift in optical loss towards lower photon energies. Nevertheless, there is a discernible blueshift in the optical loss towards higher photon energies when compressive strain appears. The optical losses for Mg_3NI_3 become greater in the visible light region when put through tensile strains instead of compressive forces [72,74].

A perovskite's reflectivity refers to how much light it reflects, either visible light or electromagnetic radiation. Composition, crystal structure, and surface form are three of the many parameters that can drastically affect the total reflectivity of perovskites. Perovskites made of Mg_3NI_3 may have distinct reflectances based on the wavelength and angle of reflection of the light that hits them. The reflectance of the Mg_3NI_3 perovskite substance may be used to estimate photon energy, as depicted in Fig. 12(a). The intensity of the reflectivity shift is most pronounced between 0 and 20 eV. At an energy of 14 eV, the reflectivity is at its highest.

Consistent with previous research, our outcomes on the visible properties of Mg_3NI_3 are presented here [79]. For visible light devices, materials exhibiting bandgaps below 3.1 eV are preferable [76]. The peculiar spectral characteristics of Mg_3NI_3 perovskite makes it an attractive material for employment in solar cells, optoelectronics, and optical sensors, among several other prospective applications.

The refractive index is an indication of a substance's permeability to received photons; it is a dimensionless integer that quantifies the

Table 3
Mechanical and elastic properties of cubic Mg_3NI_3 perovskite as estimated under different compressive and tensile strains.

Strain (%)	C_{11}	C_{12}	C_{44}	C" = C_{12}–C_{44}	B (GPa)	G (GPa)	E (GPa)	B/G	ϑ
−6	138.1	53.9	30.0	23.9	84.4	38.4	96.1	2.20	0.290
−4	105.3	47.6	27.2	20.4	70.4	32.3	79.6	2.18	0.282
−2	74.2	40.6	23.0	17.6	57.0	27.3	66.0	2.09	0.279
0	72.2	39.9	22.8	17.1	50.1	25.6	61.4	1.96	0.275
+2	65.7	38.5	22.1	16.4	47.6	24.7	61.7	1.93	0.271
+4	57.2	36.8	21.2	15.6	42.3	22.4	52.6	1.89	0.268
+6	41.7	34.2	19.8	14.4	33.1	18.2	42.1	1.82	0.266

velocity of light streaming throughout a material. equation (6) specifies the real part of a material's complex refractive index n (ω).

$$n(\omega)=\sqrt{\frac{\varepsilon_1(\omega)^2}{2}+\sqrt{\frac{\varepsilon_1(\omega)^2+\varepsilon_2(\omega)^2}{2}}} \tag{6}$$

To calculate the light-transmission capacity of the Mg_3NI_3 materials. The n(ω) refraction spectra are shown in Fig. 12(b). These materials are optically persistent, as evidenced by the photon energies appearing to hang unchanged above the band gap energy calculated by the refractive index, n. For semiconductors, the static refractive index, n (0), is an important physical trait. In comparison to Mg_3NI_3 the static refractive index has a maximum n (0) that is close to 3.16 eV. As energy levels rise, Mg_3NI_3's refractive index drops. Still, the refractive index drops to its minimum value, n = 0.313, when the incident photon's energy reaches E = 14.52 eV. This Mg_3NI_3 appeared to have separate refraction indices, corresponding to the refraction spectrum study. As expected, these findings corroborate the experience.

3.8. *Mechanical properties*

Many mechanical features of materials are defined by their elastic constants. These features include machinability, stiffness, hardness, ductile-brittle behavior, and stability. Table 3 shows the findings of the elastic constant calculations (C_{11}, C_{12}, and C_{44}) conducted assuming density functional theory (DFT) in our investigation of Mg_3NI_3. The researchers used the popular Born stability metrics, described as follows [75,76], to evaluate the mechanical stability of Mg_3NI_3:

$C_{11} > 0$, $C_{44} > 0$, $C_{11} + 2C_{12} > 0$, $C_{11}–C_{12} > 0$

Apart from that, we estimated a few mechanical characteristics, which involve Young's modulus (E), bulk modulus (B), Poisson's ratio (ϑ), Pugh's ratio (B/G), shear modulus (G), and the Cauchy pressure (C") [77]. A material's ductility and brittleness can be established by looking at its Cauchy pressure, Poisson's ratio, and Pugh's ratio. A material's ductility or brittleness is significantly impacted by the Cauchy pressure, which has been defined as C" = C_{12}–C_{44}. A ductile material exhibits a positive Cauchy pressure; when it is negative, it means it is brittle [78]. Any material with a Poisson's ratio over 0.26 and a Pugh's ratio above 1.75 qualifies as ductile. Materials are regarded as brittle when their Poisson's ratio is beneath 0.26 and their Pugh's ratio is under 1.75 [79]. The mechanical stability of Mg_3NI_3 is shown in Table 3, which displays the values for Mg_3NI_3's Young modulus (E), Shear modulus (G), Bulk modulus (B), Poisson ratio (ϑ), and Pugh's ratio (B/G). The Pugh's ratio is higher than 1.75, and the Poisson's ratio is higher than 0.26. Hence, the ductileness is revealed by Mg_3NI_3 material.

A system's directionally dependent features can be characterized using knowledge of several anisotropy indices. Due to the inherent symmetry and orientational preferences of individual molecules, solids exhibit anisotropy. In particular, researching elastic anisotropy has a lot of practical consequences in engineering and crystal physics for systems exposed to numerous levels of external stress, which contributes to enhanced mechanical durability [80–82]. The following equation (7) [83]:

$$A^U=5\frac{G_V}{G_R}+\frac{B_V}{B_R}-6\geq 0 \tag{7}$$

Where stood for the A^U, or universal anisotropic index, which was put up by Ranganathan et al. and Shiva Kumar. An isotropic state of a material can be found by analyzing its universal anisotropy (A^U) value. The Mg_3NI_3 computed A^U value demonstrates its anisotropic behavior, which is different from the isotropic behavior of a substance when A^U = 0. From these materials we evaluated, Mg_3NI_3 deviates the greatest from zero.

The proportion of anisotropy under shear (A_G) and bulk (A_B) conditions is amenable to computation by use of the subsequent formula (8, 9):

$$A_G=\frac{G_V-G_R}{G_V+G_R} \tag{8}$$

$$A_B=\frac{B_V-B_R}{B_V+B_R} \tag{9}$$

The bulk modulus (B) and the shear modulus (G), with the Voigt and Reuss approximations (V and R, respectively) are subscripted. According to Ref. [87], the material's elastic anisotropy is at its maximum when A_B = A_G = 1, and it's at its lowest when A_B = A_G = 0. For the substance in issue, the bulk modulus is isotropic, as indicated by the observed value of A_G, which in turn reveals the currently present shear anisotropy. More precise insights into elastic anisotropy have been uncovered by studying and evaluating shear anisotropy across multiple orientations at distinct crystallographic planes. The shear anisotropic factors A_i, where i ranges from 1 to 3, are defined by A_1, A_2, and A_3 in the following equations (10)–(12) [84,85]:

For {100} shear plane,

$$A_1=\frac{4C_{44}}{C_{11}+C_{33}-2C_{13}} \tag{10}$$

For {010} shear plane,

$$A_2=\frac{4C_{55}}{C_{22}+C_{33}-2C_{23}} \tag{11}$$

For {001} shear plane,

$$A_3=\frac{4C_{66}}{C_{11}+C_{22}-2C_{12}} \tag{12}$$

Gaining accurate anisotropy requires finding the Zener anisotropy index (A) and its corresponding value, the Zener anisotropy (A^{eq}). We can estimate their worth by plugging them into this equations 13 and 14 [86]:

$$A=\frac{4C_{44}}{C_{11}-C_{12}} \tag{13}$$

$$A^{eq}=\left(1+\frac{5}{12}A^U\right)+\sqrt{\left(1+\frac{5}{12}A^U\right)^2-1} \tag{14}$$

The isotropic character of a cubic structure is shown by an A = 1 and an equation: $A_1 = A_2 = A_3 = A$. In addition, the distribution from this

Table 4
Shear anisotropic factors A_i (i = 1–3), Zener's anisotropy index (A), anisotropy in shear (A_G), anisotropy in bulk modulus (A_B), universal anisotropy index (A^U), and equivalent Zener anisotropy (A^{eq}) of Mg_3NI_3 material.

Mg_3NI_3 Compound	A_1	A_2	A_3	A	A_G	A_B	A^U	A^{eq}
Without SOC	0.8350	0.8350	0.8350	1.6672	0.0070	0	0.0392	1.1975
With SOC	0.8551	0.8551	0.8551	1.7103	0.0039	0	0.0190	1.1339

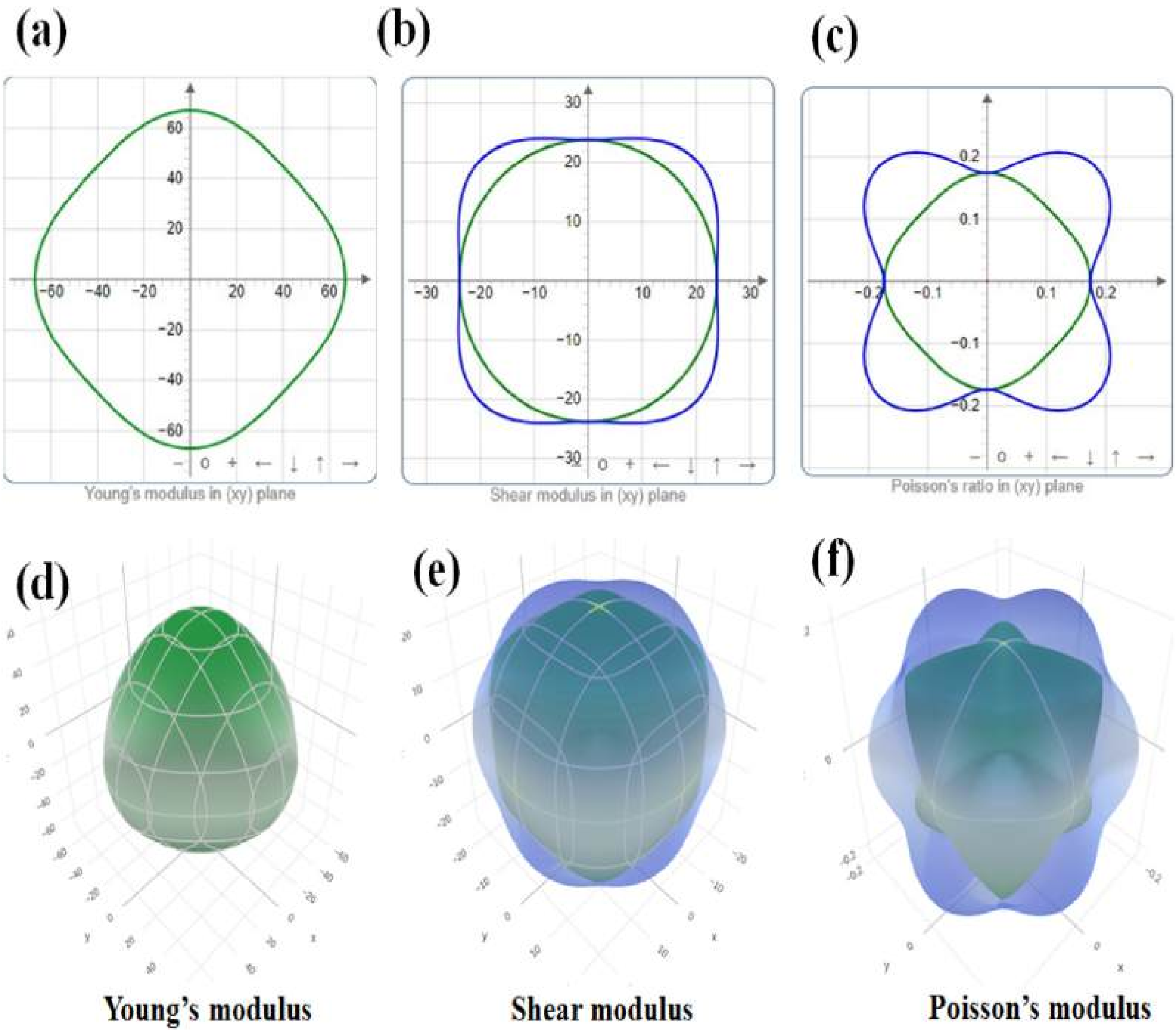

Fig. 13. The isotropy in the Young's modulus, E (GPa); Share modulus, G (GPa); Poisson's ratio, ϑ, of Mg_3NI_3 material (a) the 2D plots and (b) displays the 3D plots.

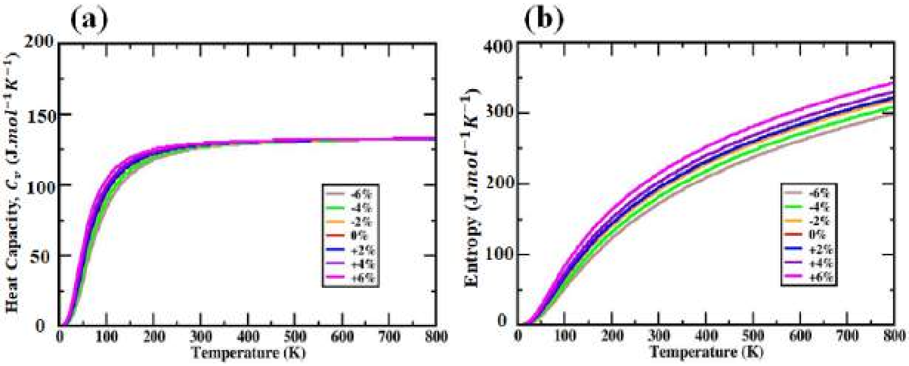

Fig. 14. (a) The heat capacity against temperature and (b) The Entropy versus temperature of Mg_3NI_3 material.

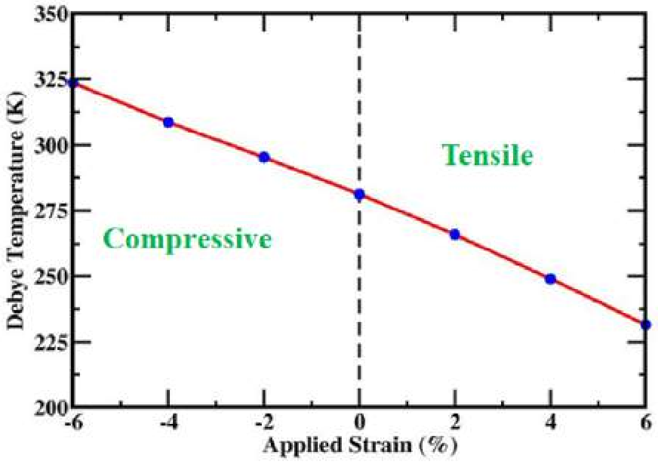

Fig. 15. At a fixed temperature 0 K, the Debye temperature varies with strain Mg_3NI_3 compound.

value denotes the anisotropy degree. The material is anisotropic, as seen in Table 4, the most pronounced anisotropic performance is exhibited, with the largest deviation. The A^{eq} adds more confirmation of its nature.

Fig. 13(a, b, c) depicts the two-dimensional (2D) framework, Fig. 13 (d, e, f) the three-dimensional (3D) for the direction dependency of the Young modulus (E) concept of the shear modulus (G), and the Poisson ratio (ϑ), respectively, for demonstrating the anisotropy. Compared to an isotropic crystal, which preserves its spherical shape, this one deviates from it, exhibiting a degree of anisotropy in numerous directions. These findings also follow the preceding discussion using different anisotropy indicators, and it is evident from Fig. 13(a, b, c) that the material superconductor exhibits an anisotropy nature.

3.9. Thermal properties

Evaluating thermal properties under extreme circumstances of heat and pressure demands the use of a quasi-harmonic Debye approximation. This static approximation distinguishes the structural parameters at $T = 0$ and $P = 0$, beginning with the projection of the total energy regarding the primitive cell volume (*E*-V). In this way, the macroscopic attributes can be determined by fitting them to T (temperature) using standard thermodynamic formulas. For the range of 0 K–800 K, thermal parameters can also be effectively estimated through the quasi-harmonic approach. Fig. 14(a) depicts the thermal effect, which is analogous to C_v, the heat capacity. The C_v convergence occurs at the volume at which Dulong and Petit's limits are reached, which is 132 J $mol^{-1}K^{-1}$. Directly proportional to T^3 is the C_v at low temperatures. For the measurement of the heat potential, which is determined by the dynamics of the atomic initiatives at intermediate temperatures [87], however, long-term inspection is important. Fig. 14(a) depicts the behavior of the C_v at a specific temperature in conjunction with strain in the Mg_3NI_3 mechanism. Also seen in Fig. 14(b) is the temperature modulation of the Mg_3NI_3 material from 0 K to 800 K. In the structure of Mg_3NI_3 the thermal entropy approaches its maximum at 800 K. We remark on the temperature sensitivity of entropy and study its variability in the existence of strain oscillations. In Fig. 14(b), we can see that as compressive strain grows, entropy falls, and tensile strain increases. At 800 K, the maximum entropy is noted, and the entropy of Mg_3NI_3 is 322 J $mol^{-1}K^{-1}$. At +6 % strain, the thermal entropy obtains its maximum value of 343 J $mol^{-1}K^{-1}$ because of the strain and the value of 298 J $mol^{-1}K^{-1}$ is the minimum at a strain of −6%.

Debye temperature υ_D varies due to the applied strain displayed in Fig. 15, when the compressive strain grows the Debye temperature rises, and due to the increasing tensile strain, the Debye temperature υ_D decreases. At −6% strain, Debye temperature υ_D is maximum, and at +6 % strain, Debye temperature υ_D is minimum.

Finally, we noticed that the Debye temperature υ_D of Mg_3NI_3 is influenced by both temperature and pressure, as shown in Fig. 16. By far the most frequently occurring cause of lattice vibration at temperatures lower than the material's Debye temperature is acoustic excitation. Right away, as the temperature rises above the Debye temperature, however, this effect becomes negligible.

$$\upsilon_D = \frac{\leftarrow}{K_B}\left(6^2 V^{\frac{1}{2}} n\right)^{\frac{1}{3}} f(\delta)\sqrt{\frac{B_s}{M}} \tag{15}$$

Equation (15) requires the following variables and constants: Boltzmann constant (k_B), adiabatic bulk modulus (B_s), volume (V), Molecular mass (M), number of atoms per primitive cell (n), and $f(\sigma)$, which is a function of Poisson's ratio. Fig. 16(a) shows that υ_D approximately constant as temperature rises from 0 K to 800 K when the pressure is constant, this characteristic is also maintained in different pressures. We also find that the Debye temperature grows when the pressure increases. The association between the applied pressure and the fluctuation of the Debye temperature appears in Fig. 16(b). We conclude that when the pressure goes up, so does the Debye temperature. This characteristic is also maintained in different temperatures.

4. Conclusion

In this study, Mg_3NI_3 is explored with regard to its structural, optical,

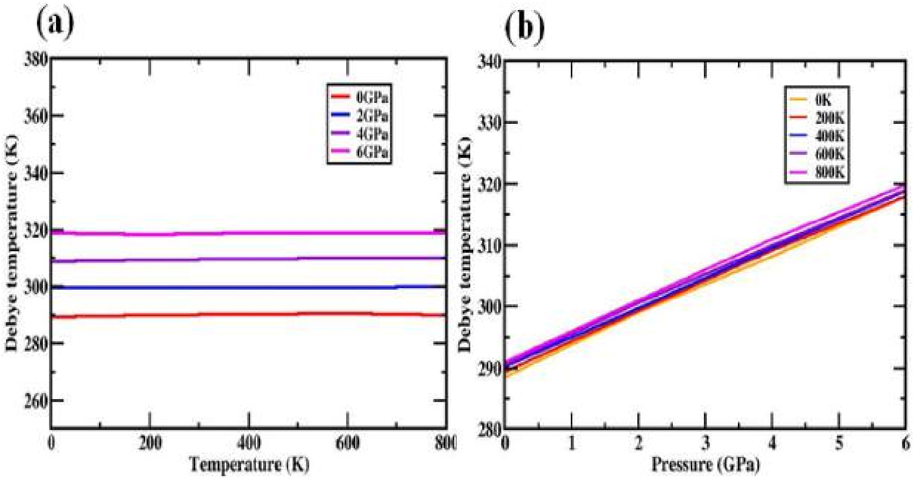

Fig. 16. At a different temperature and pressure, the Debye temperature varies with respect to pressure and temperature for Mg_3NI_3 compound.

electronic, and thermodynamical properties by using density-functional theory computations based on first principles. We have determined that the compounds of interest are stable by AIMD computation and phonon analysis. The implied lattice value of 5.60 A° points out that Mg_3NI_3 has the optimal structure. For the Mg_3NI_3 structure, a magnitude of 0.412 eV for the indirect bandgap (between Γ and R point) has been identified. Incorporating the SOC effect causes a decrease in the electrical bandgap of Mg_3NI_3 to 0.363 eV. Even if allowing for the SOC impact is removed, the fact that bandgap decreases with increasing tensile strain percentage remains unchanged. In fact, the bandgap widens as the produced compressive strain increases. Our newest findings ought to encourage more research into creating cutting-edge optoelectronic devices with Mg_3NI_3 characteristics and we couldn't be more eager regarding it. The results suggest that Mg_3NI_3 could be beneficial for optoelectronic devices.

CRediT authorship contribution statement

I.K. Gusral Ghosh Apurba: Writing – original draft, Visualization, Resources, Formal analysis, Data curation. **Md Rasidul Islam:** Writing – review & editing, Writing – original draft, Validation, Supervision, Methodology, Investigation, Conceptualization. **Md Shizer Rahman:** Writing – original draft, Project administration, Formal analysis, Data curation. **Nazia Iram:** Writing – review & editing, Software, Resources, Formal analysis. **Md Ferdous Rahman:** Writing – review & editing, Software, Resources, Methodology, Data curation. **Sohail Ahmad:** Validation, Methodology, Investigation, Funding acquisition.

Declaration of competing interest

The authors declare that they have no known competing financial interests or personal relationships that could have appeared to influence the work reported in this paper.

Data availability

Data will be made available on request.

References

[1] M.K. Hossain, G.F.I. Toki, J. Madan, R. Pandey, H. Bencherif, M.K.A. Mohammed, M.R. Islam, M.H.K. Rubel, M.F. Rahman, S. Bhattarai, A comprehensive study of the optimization and comparison of cesium halide perovskite solar cells using ZnO and Cu 2 FeSnS 4 as charge transport layers, New J. Chem. 47 (2023) 8602–8624.

[2] M.K. Hossain, M.S. Uddin, G.F.I. Toki, M.K.A. Mohammed, R. Pandey, J. Madan, M. F. Rahman, M.R. Islam, S. Bhattarai, H. Bencherif, Achieving above 24% efficiency with non-toxic CsSnI 3 perovskite solar cells by harnessing the potential of the absorber and charge transport layers, RSC Adv. 13 (2023) 23514–23537.

[3] M.K. Hossain, S. Bhattarai, A.A. Arnab, M.K.A. Mohammed, R. Pandey, M.H. Ali, M.F. Rahman, M.R. Islam, D.P. Samajdar, J. Madan, Harnessing the potential of CsPbBr 3-based perovskite solar cells using efficient charge transport materials and global optimization, RSC Adv. 13 (2023) 21044–21062.

[4] M.K. Hossain, G.F.I. Toki, I. Alam, R. Pandey, D.P. Samajdar, M.F. Rahman, M. R. Islam, M.H.K. Rubel, H. Bencherif, J. Madan, Numerical simulation and optimization of a CsPbI 3-based perovskite solar cell to enhance the power conversion efficiency, New J. Chem. 47 (2023) 4801–4817.

[5] M.K. Hossain, D.P. Samajdar, R.C. Das, A.A. Arnab, M.F. Rahman, M.H.K. Rubel, M. R. Islam, H. Bencherif, R. Pandey, J. Madan, Design and simulation of Cs2BiAgI6 double perovskite solar cells with different electron transport layers for efficiency enhancement, Energy Fuel. 37 (2023) 3957–3979.

[6] M.F. Rahman, M.H. Rahman, M.R. Islam, M.K. Hossain, A. Ghosh, M.S. Islam, M. M. Islam, M. Harun-Or-Rashid, H. Albalawi, Q. Mahmood, The optical and electronic properties of inorganic halide perovskite Sr3NCl3 under applied biaxial strain, J. Mater. Sci. 58 (2023) 13100–13117, https://doi.org/10.1007/s10853-023-08825-5.

[7] H.J. Feng, Q. Zhang, Predicting efficiencies >25% A3MX3photovoltaic materials and Cu ion implantation modification, Appl. Phys. Lett. 118 (2021), https://doi.org/10.1063/5.0039936.

[8] M.A.B. Shanto, M.F. Rahman, M.R. Islam, A. Ghosh, A. Azzouz-Rached, H. Albalawi, Q. Mahmood, Investigating how the electronic and optical properties of a novel cubic inorganic halide perovskite, Sr 3NI 3 are affected by strain, F1000Research. 12 (2023) 1005.

[9] M.F. Rahman, M.A. Rahman, M.R. Islam, A. Ghosh, B. Shanto, M. Abul, M. Chowdhury, M. Al Ijajul Islam, M.H. Rahman, M.K. Hossain, Unraveling the strain-induced and spin–orbit coupling effect of novel inorganic halide perovskites of Ca3AsI3 using DFT, AIP Adv. 13 (2023).

[10] M.R. Islam, M.R.H. Mojumder, R. Moshwan, A.S.M.J. Islam, M.A. Islam, M. S. Rahman, M.H. Kabir, Strain-driven optical, electronic, and mechanical properties of inorganic halide perovskite CsGeBr3, ECS J. Solid State Sci. Technol. 11 (2022) 33001.

[11] A. Ghosh, M.F. Rahman, M.R. Islam, M.S. Islam, M. Amami, M.K. Hossain, A.B. Md Ismail, Inorganic novel cubic halide perovskite Sr3AsI3: strain-activated electronic and optical properties, Heliyon 9 (2023) e19271, https://doi.org/10.1016/j.heliyon.2023.e19271.

[12] S. Bhattarai, M.K. Hossain, R. Pandey, J. Madan, D.P. Samajdar, M.F. Rahman, M. Z. Ansari, M. Amami, Perovskite solar cells with dual light absorber layers for performance efficiency exceeding 30, Energy Fuel. 37 (2023) 10631–10641.

[13] M.K. Hossain, M.K.A. Mohammed, R. Pandey, A.A. Arnab, M.H.K. Rubel, K. M. Hossain, M.H. Ali, M.F. Rahman, H. Bencherif, J. Madan, Numerical analysis in DFT and SCAPS-1D on the influence of different charge transport layers of CsPbBr3 perovskite solar cells, Energy Fuel. 37 (2023) 6078–6098.

[14] M.K. Hossain, A.A. Arnab, D.P. Samajdar, M.H.K. Rubel, M.M. Hossain, M.R. Islam, R.C. Das, H. Bencherif, M.F. Rahman, J. Madan, Design insights into La2NiMnO6-based perovskite solar cells employing different charge transport layers: DFT and SCAPS-1D frameworks, Energy Fuel. 37 (2023) 13377–13396.

[15] M.M.A. Moon, M.H. Ali, M.F. Rahman, A. Kuddus, J. Hossain, A.B.M. Ismail, Investigation of thin-film p-BaSi2/n-CdS heterostructure towards semiconducting silicide based high efficiency solar cell, Phys. Scripta. 95 (2020) 35506.

[16] M.F. Rahman, M.J.A. Habib, M.H. Ali, M.H.K. Rubel, M.R. Islam, A.B. Md Ismail, M.K. Hossain, Design and numerical investigation of cadmium telluride (CdTe) and iron silicide (FeSi2) based double absorber solar cells to enhance power conversion efficiency, AIP Adv. 12 (2022).

[17] M.M.A. Moon, M.F. Rahman, M. Kamruzzaman, J. Hossain, A.B.M. Ismail, Unveiling the prospect of a novel chemical route for synthesizing solution-processed CdS/CdTe thin-film solar cells, Energy Rep. 7 (2021) 1742–1756.

[18] A. Isha, A. Kowsar, A. Kuddus, M.K. Hossain, M.H. Ali, M.D. Haque, M.F. Rahman, High efficiency Cu2MnSnS4 thin film solar cells with SnS BSF and CdS ETL layers: a numerical simulation, Heliyon 9 (2023) e15716.

[19] M.M.A. Moon, M.H. Ali, M.F. Rahman, J. Hossain, A.B.M. Ismail, Design and simulation of FeSi2-based novel heterojunction solar cells for harnessing visible and near-infrared light, Phys. Status Solidi. 217 (2020) 1900921.

[20] M.F. Rahman, M.M.A. Moon, M.K. Hossain, M.H. Ali, M.D. Haque, A. Kuddus, J. Hossain, A.B.M. Ismail, Concurrent investigation of antimony chalcogenide (Sb2Se3 and Sb2S3)-based solar cells with a potential WS2 electron transport layer, Heliyon 8 (2022) e15716.

[21] H. Absike, N. Baaalla, R. Lamouri, H. Labrim, H. Ez-zahraouy, Optoelectronic and photovoltaic properties of Cs2AgBiX6 (X= Br, Cl, or I) halide double perovskite for solar cells: insight from density functional theory, Int. J. Energy Res. 46 (2022) 11053–11064.

[22] I. Hamideddine, N. Tahiri, O. El Bounagui, H. Ez-Zahraouy, Ab initio study of structural and optical properties of the halide perovskite KBX3 compound, J. Korean Ceram. Soc. 59 (2022) 350–358.

[23] I. Hamideddine, H. Zitouni, N. Tahiri, O. El Bounagui, H. Ez-Zahraouy, A DFT study of the electronic structure, optical, and thermoelectric properties of halide perovskite KGeI 3-x Br x materials: photovoltaic applications, Appl. Phys. A 127 (2021) 1–7.

[24] H.-J. Wu, Q. Yang, C.-E. Hu, Y. Cheng, G.-F. Ji, Structural, elastic, electronic and optical properties of double perovskites Ba2NaXO6 (X= Cl, Br, I): first-principles study, Mater. Sci. Semicond. Process. 153 (2023) 107165.

[25] N. Tahiri, S. Dahbi, I. Dani, O. El Bounagui, H. Ez-Zahraouy, Magnetic, magnetocaloric and thermoelectric investigations of perovskite LaFeO3 compound: first principles and Monte Carlo calculations, Comput. Theor. Chem. 1204 (2021) 113421.

[26] H. Zitouni, N. Tahiri, O. El Bounagui, H. Ez-Zahraouy, Electronic, optical and transport properties of perovskite BaZrS3 compound doped with Se for photovoltaic applications, Chem. Phys. 538 (2020) 110923.

[27] Y. Wang, X. Liu, T. Zhang, X. Wang, M. Kan, J. Shi, Y. Zhao, The role of dimethylammonium iodide in CsPbI3 perovskite fabrication: additive or dopant? Angew. Chem. 131 (2019) 16844–16849.

[28] Y. Wang, T. Zhang, M. Kan, Y. Zhao, Bifunctional stabilization of all-inorganic α-CsPbI3 perovskite for 17% efficiency photovoltaics, J. Am. Chem. Soc. 140 (2018) 12345–12348.

[29] Best Research-Cell Efficiencies, 2024, p. 2025.

[30] Y.-Q. Zhao, Q.-R. Ma, B. Liu, Z.-L. Yu, M.-Q. Cai, Pressure-induced strong ferroelectric polarization in tetra-phase perovskite CsPbBr 3, Phys. Chem. Chem. Phys. 20 (2018) 14718–14724.

[31] Y.-Q. Zhao, B. Liu, Z.-L. Yu, D. Cao, M.-Q. Cai, Tuning charge carrier types, superior mobility and absorption in lead-free perovskite CH3NH3GeI3: theoretical study, Electrochim. Acta 247 (2017) 891–898.

[32] P. Wang, J. Guan, D.T.K. Galeschuk, Y. Yao, C.F. He, S. Jiang, S. Zhang, Y. Liu, M. Jin, C. Jin, Pressure-induced polymorphic, optical, and electronic transitions of formamidinium lead iodide perovskite, J. Phys. Chem. Lett. 8 (2017) 2119–2125.

[33] Y. Nagaoka, K. Hills-Kimball, R. Tan, R. Li, Z. Wang, O. Chen, Nanocube superlattices of cesium lead bromide perovskites and pressure-induced phase transformations at atomic and mesoscale levels, Adv. Mater. 29 (2017) 1606666.

[34] Q. Li, S. Li, K. Wang, Z. Quan, Y. Meng, B. Zou, High-pressure study of perovskite-like organometal halide: band-gap narrowing and structural evolution of [NH3-(CH2) 4-NH3] CuCl4, J. Phys. Chem. Lett. 8 (2017) 500–506.

[35] A. Jaffe, Y. Lin, W.L. Mao, H.I. Karunadasa, Pressure-induced metallization of the halide perovskite (CH3NH3) PbI3, J. Am. Chem. Soc. 139 (2017) 4330–4333.

[36] J.C. Beimborn, L.R. Walther, K.D. Wilson, J.M. Weber, Size-dependent pressure-response of the photoluminescence of CsPbBr3 nanocrystals, J. Phys. Chem. Lett. 11 (2020) 1975–1980.
[37] A. El Badraoui, S. Dahbi, N. Tahiri, O. El Bounagui, H. Ez-Zahraouy, Electronic structure, optical, and thermoelectric properties of AgTaO3− XYX (Y= S, Se, or Te) perovskite for photovoltaic applications: a DFT study, Micro and Nanostructures. 174 (2023) 207475.
[38] N. Ennassiri, N. Tahiri, O. El Bounagui, H. Ez-Zahraouy, A. Benyoussef, Structural, electronic, magnetic, and magnetocaloric properties in metallic antiperovskite compound Mn3GaC, Mater. Res. Bull. 98 (2018) 335–339.
[39] N. Ennassiri, N. Tahiri, O. El Bounagui, H. Ez-Zahraouy, A. Benyoussef, Magnetic, magnetocaloric and transport properties in AlCMn3 antiperovskite compound, J. Alloys Compd. 741 (2018) 1196–1202.
[40] S. Dahbi, N. Tahiri, O. El Bounagui, H. Ez-Zahraouy, Chalcogens' impurities and a single F-center in perovskite SrHfO3 compound: ab initio calculations, Mater. Sci. Semicond. Process. 138 (2022) 106271.
[41] M.G. Elmahgary, A.M. Mahran, M. Ganoub, S.O. Abdellatif, Optical investigation and computational modelling of BaTiO3 for optoelectronic devices applications, Sci. Rep. 13 (2023) 4761.
[42] M. Roknuzzaman, K.K. Ostrikov, K.C. Wasalathilake, C. Yan, H. Wang, T. Tesfamichael, Insight into lead-free organic-inorganic hybrid perovskites for photovoltaics and optoelectronics: a first-principles study, Org. Electron. 59 (2018) 99–106.
[43] M.F. Rahman, M.A. Rahman, M.R. Islam, A. Ghosh, M.A. Bashar Shanto, M. Chowdhury, M. Al Ijajul Islam, M.H. Rahman, M.K. Hossain, M.A. Islam, Unraveling the strain-induced and spin–orbit coupling effect of novel inorganic halide perovskites of Ca3AsI3 using DFT, AIP Adv. 13 (2023) 85329, https://doi.org/10.1063/5.0156961.
[44] M.A. Brogan, R.W. Hughes, R.I. Smith, D.H. Gregory, Structural studies of magnesium nitride fluorides by powder neutron diffraction, J. Solid State Chem. 185 (2012) 213–218.
[45] H.J. Monkhorst, J.D. Pack, Special points for Brillouin-zone integrations, Phys. Rev. B 13 (1976) 5188.
[46] P. Giannozzi, O. Andreussi, T. Brumme, O. Bunau, M.B. Nardelli, M. Calandra, R. Car, C. Cavazzoni, D. Ceresoli, M. Cococcioni, Advanced capabilities for materials modelling with Quantum ESPRESSO, J. Phys. Condens. Matter 29 (2017) 465901.
[47] J.P. Perdew, A. Zunger, Self-interaction correction to density-functional approximations for many-electron systems, Phys. Rev. B 23 (1981) 5048.
[48] P. Giannozzi, S. Baroni, N. Bonini, M. Calandra, R. Car, C. Cavazzoni, D. Ceresoli, G.L. Chiarotti, M. Cococcioni, I. Dabo, Quantum espresso: a modular and open-source software project for quantum simulations of materials, J. Phys. Condens. Matter 21 (2009) 395502.
[49] F. Karsch, A. Patkos, P. Petreczky, Screened perturbation theory, Phys. Lett. B 401 (1997) 69–73.
[50] M.H.K. Rubel, M.A. Hossain, M.K. Hossain, K.M. Hossain, A.A. Khatun, M. M. Rahaman, M.F. Rahman, M.M. Hossain, J. Hossain, First-principles calculations to investigate structural, elastic, electronic, thermodynamic, and thermoelectric properties of CaPd3B4O12 (B= Ti, V) perovskites, Results Phys. 42 (2022) 105977.
[51] M.A. Rahman, F. Mostari, M.Z. Hasan, A. Irfan, M.F. Rahman, M.J. Hosain, S. C. Mouna, I.A. Chowdhury, M. Rasheduzzaman, M.S.H. Choudhury, First principles study on the structural, elastic, electronic, optical and thermal properties of lead-free perovskites CsCaX3 (X= F, Cl, Br), Phys. B Condens. Matter 669 (2023) 415260.
[52] D.C. Langreth, M.J. Mehl, Beyond the local-density approximation in calculations of ground-state electronic properties, Phys. Rev. B 28 (1983) 1809.
[53] J. Yang, L.Z. Tan, A.M. Rappe, Hybrid functional pseudopotentials, Phys. Rev. B 97 (2018) 85130.
[54] N. Ashari-Astani, S. Meloni, A.H. Salavati, G. Palermo, M. Grätzel, U. Rothlisberger, Computational characterization of the dependence of halide perovskite effective masses on chemical composition and structure, J. Phys. Chem. C 121 (2017) 23886–23895, https://doi.org/10.1021/acs.jpcc.7b04898.
[55] N.J.J. De Klerk, I. Rosłoń, M. Wagemaker, Diffusion mechanism of Li argyrodite solid electrolytes for Li-ion batteries and prediction of optimized halogen doping: the effect of Li vacancies, halogens, and halogen disorder, Chem. Mater. 28 (2016) 7955–7963.
[56] Z. Deng, Z. Zhu, I.-H. Chu, S.P. Ong, Data-driven first-principles methods for the study and design of alkali superionic conductors, Chem. Mater. 29 (2017) 281–288.
[57] L. Zhou, K.-H. Park, X. Sun, F. Lalère, T. Adermann, P. Hartmann, L.F. Nazar, Solvent-engineered design of argyrodite Li6PS5X (X= Cl, Br, I) solid electrolytes with high ionic conductivity, ACS Energy Lett. 4 (2018) 265–270.
[58] S. Boulineau, M. Courty, J.-M. Tarascon, V. Viallet, Mechanochemical synthesis of Li-argyrodite Li6PS5X (X= Cl, Br, I) as sulfur-based solid electrolytes for all solid state batteries application, Solid State Ionics 221 (2012) 1–5.
[59] P. Adeli, J.D. Bazak, K.H. Park, I. Kochetkov, A. Huq, G.R. Goward, L.F. Nazar, Boosting solid-state diffusivity and conductivity in lithium superionic argyrodites by halide substitution, Angew. Chem. Int. Ed. 58 (2019) 8681–8686.
[60] P. Adeli, J.D. Bazak, A. Huq, G.R. Goward, L.F. Nazar, Influence of aliovalent cation substitution and mechanical compression on Li-ion conductivity and diffusivity in argyrodite solid electrolytes, Chem. Mater. 33 (2020) 146–157.
[61] C. Yu, F. Zhao, J. Luo, L. Zhang, X. Sun, Recent development of lithium argyrodite solid-state electrolytes for solid-state batteries: synthesis, structure, stability and dynamics, Nano Energy 83 (2021) 105858.
[62] C. Yu, S. Ganapathy, J. Hageman, L. Van Eijck, E.R.H. Van Eck, L. Zhang, T. Schwietert, S. Basak, E.M. Kelder, M. Wagemaker, Facile synthesis toward the optimal structure-conductivity characteristics of the argyrodite Li6PS5Cl solid-state electrolyte, ACS Appl. Mater. Interfaces 10 (2018) 33296–33306.
[63] H. Deiseroth, S. Kong, H. Eckert, J. Vannahme, C. Reiner, T. Zaiß, M. Schlosser, Li6PS5X: a class of crystalline Li-rich solids with an unusually high Li+ mobility, Angew. Chem. 120 (2008) 767–770.
[64] M.A. Kraft, S.P. Culver, M. Calderon, F. Böcher, T. Krauskopf, A. Senyshyn, C. Dietrich, A. Zevalkink, J. Janek, W.G. Zeier, Influence of lattice polarizability on the ionic conductivity in the lithium superionic argyrodites Li6PS5X (X= Cl, Br, I), J. Am. Chem. Soc. 139 (2017) 10909–10918.
[65] R.P. Rao, S. Adams, Studies of lithium argyrodite solid electrolytes for all-solid-state batteries, Phys. Status Solidi. 208 (2011) 1804–1807.
[66] M.K. Hossain, A.A. Arnab, R.C. Das, K.M. Hossain, M.H.K. Rubel, M.F. Rahman, H. Bencherif, M.E. Emetere, M.K.A. Mohammed, R. Pandey, Combined DFT, SCAPS-1D, and wxAMPS frameworks for design optimization of efficient Cs 2 BiAgI 6-based perovskite solar cells with different charge transport layers, RSC Adv. 12 (2022) 35002–35025.
[67] M.K. Hossain, M.H.K. Rubel, G.F.I. Toki, I. Alam, M.F. Rahman, H. Bencherif, Effect of various electron and hole transport layers on the performance of CsPbI3-based perovskite solar cells: a numerical investigation in DFT, SCAPS-1D, and wxAMPS frameworks, ACS Omega 7 (2022) 43210–43230.
[68] M.K. Hossain, G.F. Ishraque Toki, D.P. Samajdar, M.H.K. Rubel, M. Mushtaq, M. R. Islam, M.F. Rahman, S. Bhattarai, H. Bencherif, M.K.A. Mohammed, Photovoltaic performance investigation of Cs3Bi2I9-based perovskite solar cells with various charge transport channels using DFT and SCAPS-1D frameworks, Energy Fuel. 37 (2023) 7380–7400.
[69] B. Ehrler, E. Alarcón-Lladó, S.W. Tabernig, T. Veeken, E.C. Garnett, A. Polman, Photovoltaics reaching for the shockley-queisser limit, ACS Energy Lett. 5 (2020) 3029–3033, https://doi.org/10.1021/acsenergylett.0c01790.
[70] A.P. Nayak, T. Pandey, D. Voiry, J. Liu, S.T. Moran, A. Sharma, C. Tan, C.H. Chen, L.J. Li, M. Chhowalla, J.F. Lin, A.K. Singh, D. Akinwande, Pressure-dependent optical and vibrational properties of monolayer molybdenum disulfide, Nano Lett. 15 (2015) 346–353, https://doi.org/10.1021/nl5036397.
[71] M. Lal, S. Kapila, Structural, electronic, optical and mechanical properties of CsCaCl3 and KCdF3 cubic perovskites, Int. J. Mater. Sci. 12 (2017).
[72] R. Islam, K. Liu, Z. Wang, S. Hasan, Y. Wu, S. Qu, Z. Wang, Strain-induced electronic and optical properties of inorganic lead halide perovskites APbBr3 (A= Rb and Cs), Mater. Today Commun. 31 (2022) 103305, https://doi.org/10.1016/j.mtcomm.2022.103305.
[73] Z. Xie, L. Hui, J. Wang, Z. Chen, C. Li, Electronic and optical properties of monolayer black phosphorus induced by bi-axial strain, Comput. Mater. Sci. 144 (2018) 304–314.
[74] M.R. Islam, A.S.M.J. Islam, K. Liu, Z. Wang, S. Qu, C. Zhao, X. Wang, Z. Wang, Strain-induced tunability of the optoelectronic properties of inorganic lead iodide perovskites APbI3 (A= Rb and Cs), Phys. B Condens. Matter 638 (2022) 413960.
[75] C. Lin, M. Zhu, Z. Cao, Y. Lin, J. Huang, J. Wu, Z. Zhou, W. Song, P. Peng, M.J. Tan, The influence of hydrogen on phase stability, mechanical and electronic properties of B2–ZrCu compound from first-principles, Int. J. Hydrogen Energy 48 (2023) 40088–40100.
[76] M. Born, On the stability of crystal lattices. I, in: Math. Proc. Cambridge Philos. Soc., Cambridge University Press, 1940, pp. 160–172.
[77] S.F. Pugh, XCII. Relations between the elastic moduli and the plastic properties of polycrystalline pure metals, Dublin Philos. Mag. J. Sci. 45 (1954) 823–843. London, Edinburgh.
[78] D.G. Pettifor, Theoretical predictions of structure and related properties of intermetallics, Mater. Sci. Technol. 8 (1992) 345–349.
[79] Y. Zhang, H. Wang, X. Wang, X. Zhang, Y. Gao, Comparison of the physical properties and electronic structure of Nb2B3 and Ta2B3, Coatings 13 (2023) 1302.
[80] R. Majumder, S.K. Mitro, B. Bairagi, Influence of metalloid antimony on the physical properties of palladium-based half-Heusler compared to the metallic bismuth: a first-principle study, J. Alloys Compd. 836 (2020) 155395.
[81] M.A. Sarker, M.M. Hasan, M. Al Momin, A. Irfan, M.R. Islam, A. Sharif, Band gap engineering in lead free halide cubic perovskites GaGeX 3 (X = Cl, Br, and I) based on first-principles calculations, RSC Adv. 14 (2024) 9805–9818, https://doi.org/10.1039/d4ra00224e.
[82] M.H.K. Rubel, S.K. Mitro, M.K. Hossain, K.M. Hossain, M.M. Rahaman, J. Hossain, B.K. Mondal, A. Akter, M.F. Rahman, I. Ahmed, A.K.M.A. Islam, First-principles calculations to investigate physical properties of single-cubic (Ba0.82K0.18)(Bi0.53Pb0.47)O3 novel perovskite superconductor, Mater, Today Commun. 33 (2022) 104302, https://doi.org/10.1016/j.mtcomm.2022.104302.
[83] D.H. Chung, W.R. Buessem, The elastic anisotropy of crystals, J. Appl. Phys. 38 (1967) 2010–2012.
[84] X. Gao, Y. Jiang, R. Zhou, J. Feng, Stability and elastic properties of Y–C binary compounds investigated by first principles calculations, J. Alloys Compd. 587 (2014) 819–826.
[85] P. Ravindran, L. Fast, P.A. Korzhavyi, B. Johansson, J. Wills, O. Eriksson, Density functional theory for calculation of elastic properties of orthorhombic crystals: application to TiSi 2, J. Appl. Phys. 84 (1998) 4891–4904.
[86] Z. Sun, S. Li, R. Ahuja, J.M. Schneider, Calculated elastic properties of M2AlC (M= Ti, V, Cr, Nb and Ta), Solid State Commun. 129 (2004) 589–592.
[87] X. Chang, W. Li, L. Zhu, H. Liu, H. Geng, S. Xiang, J. Liu, H. Chen, Carbon-based CsPbBr3 perovskite solar cells: all-ambient processes and high thermal stability, ACS Appl. Mater. Interfaces 8 (2016) 33649–33655.
[88] H.-J. Feng, Q. Zhang, Supplementary Material Predicting Efficiencies>25% A 3 MX 3 Photovoltaic Materials and Cu Ion Implantation Modification, (n.d.).